INTERNATIONAL JOURNAL FOR NUMERICAL METHODS IN FLUIDS, VOL. 17, 75–97 (1993)

A GLOBAL APPROACH TO ERROR ESTIMATION AND PHYSICAL DIAGNOSTICS IN MULTIDIMENSIONAL COMPUTATIONAL FLUID DYNAMICS

D. C. HAWORTH, S. H. EL TAHRY AND M. S. HUEBLER

Thermosciences Department, General Motors Research, 30500 Mound Road, Warren, MI 48090-9055, U.S.A.

SUMMARY

An approach for simultaneously assessing numerical accuracy and extracting physical information from multidimensional calculations of complex (engineering) flows is proposed and demonstrated. The method is based on global balance equations, i.e. volume-integrated partial differential equations for primary or derived physical quantities of interest. Balances can be applied to the full computational domain or to any subdomain down to the single-cell level. Applications to in-cylinder flows in reciprocating engines are used for illustration. It is demonstrated that comparison of the relative magnitude of the terms in the balances provides insight into the physics of the flow being computed. Moreover, for quantities that are not conserved at the cell or control volume level in the construction of the numerical scheme, the imbalance allows a direct assessment of numerical accuracy in a single run using a single mesh. The mean kinetic energy imbalance is shown to be a particularly sensitive indicator of numerical accuracy. This simple and powerful diagnostic approach can be implemented for finite-difference, finite-volume or finite-element methods.

KEY WORDS Computational fluid dynamics Error estimates Diagnostics

1. INTRODUCTION

In many applications, multidimensional computational fluid dynamics (CFD) is emerging from research status to become an engineering tool. This transition has been fuelled by the rapidly declining cost-to-performance ratio of computer hardware, by advances in interactive pre- and post-processing software, and by progress in numerical algorithms and physical submodels that enables the computation of complex flows typical of engineering applications. In the automotive industry, CFD is being applied (among other things) to in-cylinder flows in reciprocating engines to generate new insight into physical processes occurring inside the engine cylinder,[1–4] to generate generic design guidelines through parametric studies, and to analyse and suggest improvements to specific engine designs;[5] most applications of the latter type remain proprietary.

Computational capabilities often strain diagnostic capacity. While impressive graphics are routinely presented, quantitative analysis to extract the wealth of information that is implicit in multidimensional calculations generally has not kept pace with our capacity to compute ever more complex flows. At the same time, measures of numerical accuracy are needed to provide an indication of the degree to which the computed results are faithful to the underlying (modelled) partial differential equations. Continued progress in the modelling of flows such as those in the cylinder of a reciprocating internal combustion engine demands that numerical accuracy be

0271–2091/93/130075–23$16.50

Received November 1991
Revised February 1993

quantified and isolated from submodel performance (e.g. turbulence, turbulent combustion and fuel-spray models).

It is the purpose of this paper to introduce and demonstrate the utility of a simple yet powerful diagnostic approach that can be applied to assess numerical accuracy and to yield insight into physical processes. This approach is intended for application to complex engineering flows in particular, and may eventually provide the basis for an adaptive gridding scheme.

The remainder of the paper is organized as follows. Section 2 provides further background on the issues of numerical accuracy and physical diagnostics. Balance equations are introduced in Section 3. In Section 4, the CFD code in which the balances have been implemented is described. Example results for two in-cylinder configurations are presented in Section 5, and finally, results are discussed and conclusions are drawn in Section 6. An appendix contains details of the balance equations.

2. BACKGROUND

Numerical accuracy diagnostics

Low-order numerical methods and simple physical submodels (e.g. the two-equation k–ε turbulence model) contribute to the robustness and computational efficiency that are required of an engineering CFD code. However, this same robustness and speed make it imperative that error estimates be available so that plausible-looking results are not confused with accurate results, even if it is trends rather than absolute values that one is interested in capturing. A second motivation for providing error estimates is to separate numerics from the influence of modelling assumptions. Because it is difficult to isolate numerical accuracy from model performance in complex flows, numerically generated flow phenomena may erroneously be attributed to physical submodel behaviour, leading to specious model development and calibration exercises. Numerical accuracy has been cited by modellers in diverse disciplines as an issue in the development and application of advanced turbulence models to three-dimensional flows of practical interest.[6–8]

Formal error estimates for grid-based numerical schemes may be based on Taylor-series expansions[9] or Fourier analysis.[10] These analytic approaches are valuable in the development and evaluation of numerical methods for model problems. The usual method for assessing numerical accuracy in complex flows (in cases where it has been assessed at all) is through grid refinement. In this approach computations are repeated on progressively finer (or coarser) meshes and resolution is presumed to be adequate when results do not change significantly with mesh density. Estimates of the local converged solution can be made by extrapolating solutions obtained on two or more grids.

Clearly systematic grid refinement is a valid approach to error estimation. It is, in fact, the basis for evaluating the present balance approach in the examples cited in Section 5. However, the routine application of grid refinement to 'production' CFD is problematic for several reasons. (1) The leading-order term in a Taylor-series analysis of a spatial discretization scheme provides a meaningful estimate of convergence rate only in the limit as the grid spacing approaches zero. Extrapolation to zero mesh spacing of results computed on two or more finite-resolution grids will be misleading outside of this 'radius of convergence'. One cannot know *a priori* if a given mesh and numerical scheme lie within this limit; a single-run, single-mesh measure of numerical accuracy is needed. An example is given in Section 5 where even for a relatively simple flow (and axisymmetric, simple orthogonal grids), grid refinement on meshes that normally had been considered to be adequate yields misleading estimates of the converged solution. (2) Meshes for three-dimensional time-dependent internal flow problems such as in-cylinder flow in a reciprocat-

ing engine rarely exceed 250 000 grid points; more usual is CFD on grids an order of magnitude coarser. Even a 1000 000-cell mesh represents a nominal grid spacing of just 100 cells per spatial direction. For an in-cylinder problem, this corresponds to cells of about 1 mm^3, barely adequate to resolve the turbulence integral length scale. The difficulty of grid generation and the magnitude of computational resources required for such problems preclude the routine use of grid-sensitivity tests. Again, single-run assessments of numerical accuracy are needed. (3) In complex geometric configurations, numerical errors resulting from non-uniform spatial distribution of grid points and strong departures from grid orthogonality are more difficult to quantify than errors due to grid spacing alone. Systematic assessment of grid-sensitivity in such cases demands that both mesh topology and mesh density be varied. Mesh topology is often difficult to change for practical internal flow configurations.

In the present work, balances of numerically non-conserved quantities (i.e. quantities that are not conserved at the cell or control volume level in the construction of the numerical scheme) provide the basis for numerical error estimates. By comparing the magnitude of individual terms in the volume-integrated balance equation for a non-conserved flow variable with the difference between the right- and left-hand sides of the equation, the relative magnitude of numerical error compared to physical effects can be assessed directly. Positive aspects of this approach are (1) it is independent of the numerical method (finite-difference versus finite-volume versus finite-element method) and of the order of the differencing scheme (e.g. upwind versus central differencing); (2) it can be performed over the full computational domain or over any subdomain down to the level of individual cells, or simultaneously over several levels; (3) it is readily implemented for complex flows; and (4) it provides a direct assessment of accuracy in a single run. For finite-element methods, residual-based local and global error estimates can be made,[11] but no comparable measures are available for finite-difference or finite-volume methods.* Clearly, global balances do not capture all manifestations of numerical inaccuracy. Here the intent is to ensure that low-order spatial discretization error (primarily numerical diffusion) is small compared to dominant physical processes. That this approach does provide useful insight is demonstrated by the examples in Section 5. Global balances were used in a limited sense as diagnostics of numerical accuracy in earlier work.[3,12]

Physical diagnostics

Because of the overwhelming quantity of information generated in three-dimensional CFD, recent emphasis in post-processing has been in interactive graphics.[13,14] Quantitative analysis has often been limited to a small number of problem-dependent global quantities (e.g. total angular momentum and turbulence level for in-cylinder flows[1,3]); at the other extreme are flow topology diagnostics for fundamental studies of hydrodynamics.[15,16] A level of diagnostics intermediate between global parameters and three-dimensional vector fields and topology maps is needed to exploit more fully the wealth of physical information implicit in engineering computations. (Here it is understood that results are 'physical' to within the limits of the models being used.) Global balances provide tractable intermediate-level information on the contribution of different physical processes in the flow domain.

The same volume-averaged balance equations that are used to assess numerical accuracy also provide physical information. Local budgets of turbulence kinetic energy production and other modelled processes have been employed in the evaluation of turbulence models by many authors.[17,18] Global turbulence kinetic energy balances have been applied to in-cylinder flows by

* Preliminary work suggests that equivalent estimates can be constructed for finite-volume methods.

Gosman *et al.*[1] to investigate turbulence production by tumbling motion (rotation of the in-cylinder fluid about an axis normal to the cylinder axis). This analysis was expanded by Haworth *et al.*[3] who invoked budgets of in-cylinder angular momentum and mean turbulence kinetic energy to investigate induction-generated flows and turbulence production for four different intake configurations. In the present paper, a systematic development of global balances as a tool for extracting physical information and for estimating numerical accuracy is presented.

3. BALANCE EQUATIONS

We begin with the partial differential equation governing a flow variable of interest $\Phi = \Phi(\underline{x}, t)$. Here Φ can represent mass, a component of linear or angular momentum, a species mass fraction, kinetic energy or any other quantity of interest,

$$\frac{\partial \Phi}{\partial t} + \frac{\partial \Phi U_j}{\partial x_j} = \frac{\partial R_{1j}}{\partial x_j} + R_2. \tag{1}$$

Here U_j is the jth component of fluid velocity. The terms on the right-hand side have been decomposed into a contribution $\underline{R}_1$ that is expressed as a divergence-of-a-flux and a non-divergence contribution R_2. Further decomposition is often appropriate to distinguish among physical processes or contributions from different boundaries (see appendix and Section 5). By integrating equation (1) over a time-dependent volume $V(t)$ (the computational domain or a subdomain) and manipulating the result, a balance equation results:

$$\frac{\mathrm{d}}{\mathrm{d}t}\int_{V(t)} \Phi \, \mathrm{d}\tau + \int_{S(t)} \Phi U_{\mathrm{rel}\,j} \, \mathrm{d}A_j = \int_{S(t)} R_{1j} \, \mathrm{d}A_j + \int_{V(t)} R_2 \, \mathrm{d}\tau. \tag{2}$$

The notation is the same as that introduced in the appendix: $\mathrm{d}\tau$ represents a volume element in $V(t)$, $S(t)$ is the (deforming) surface of $V(t)$ with outward-pointing surface-element vector $\mathrm{d}\mathbf{A}$ and $U_{\mathrm{rel}\,j}$ is the jth component of the fluid velocity relative to the moving boundary.

The imbalance $\Delta\dot{\Phi}$ is taken to be the difference between the left- and right-hand sides of equation (2),

$$\Delta\dot{\Phi} \equiv \frac{\mathrm{d}}{\mathrm{d}t}\int_{V(t)} \Phi \, \mathrm{d}\tau + \int_{S(t)} \Phi \, U_{\mathrm{rel}\,j} \, \mathrm{d}A_j - \int_{S(t)} R_{1j} \, \mathrm{d}A_j - \int_{V(t)} R_2 \, \mathrm{d}\tau. \tag{3}$$

Clearly, $\Delta\dot{\Phi}$ is identically equal to zero. However, in a numerical representation of equation (1), $\Delta\dot{\Phi}_{\mathrm{num}}$ is non-zero unless the numerical scheme has been constructed specifically in a manner that conserves Φ at the cell or control volume level. While most CFD codes conserve the primary quantities that are being solved for (usually density or mass and linear momentum), fewer conserve derived quantities such as angular momentum and kinetic energy. In the limit of a converged numerical solution, all primary and derived quantities are conserved: hence imbalances in angular momentum, kinetic energy and higher moments can be expected to reflect numerical inaccuracy.

Numerical schemes that conserve angular momentum have been constructed and implemented.[12,19] Similarly, one might construct methods that conserve kinetic energy or other quantities of special interest in particular applications. However, all physical quantities (e.g. all moments of linear momentum) cannot be conserved simultaneously; in any numerical approach there will be non-conserved quantities to serve as candidates for numerical accuracy assessment.

The behaviour of the imbalance term in equation (3) can vary depending on the quantity Φ. For example, the energy-dissipating nature of the truncation error for convective discretizations

including standard upwind, third-order upwind and non-linear monotone methods has been established elsewhere.[9,20,21] This provides a sound basis for expecting the imbalance in mean kinetic energy to behave as a dissipation term ($\Delta\dot{\Phi}_{num}<0$, $|\Delta\dot{\Phi}_{num}|$ decreasing with improving spatial resolution) for these schemes. For other numerical methods or other physical quantities, the imbalance can be of either sign; one can say only that the imbalance approaches zero in the limit of a converged solution. A single non-negative modulus can be defined as in equation (16), for example.

Global balance equations for linear momentum, angular momentum, mean kinetic energy and turbulence kinetic energy are given in the appendix. For purposes of illustration, these equations have been derived for Favre-averaged mean quantities in the context of a k–ε turbulence model, but the approach is applicable to any set of partial differential equations.

4. FLOW CODE

While the balances are generic, it is imperative that the discretizations used to approximate the integrals in equation (3) small be consistent with the discretization scheme used to solve the governing partial differential equations (equation (1)). If the two are not compatible, large numerical errors may result, confounding attempts to extract meaningful information from the balances. Some details of the solution procedures are thus germane to interpretation of the results.

In the code used for this study, an unstructured mesh of hexahedral 'brick' elements is used to discretize the field equations in a finite-volume formulation.[22] Turbulent flow is treated conventionally by solving for ensemble-averaged variables with a two-equation k–ε turbulence model.[23] The equations solved are the compressible, time-dependent, Favre-averaged equations for momentum, pressure, internal energy, species transport, turbulence kinetic energy k and the viscous dissipation rate of turbulence kinetic energy ε. Density is specified using an equation of state.

A parameter γ controls the blend of standard upwind and central differencing for the convective terms in the mean momentum equations such that $\gamma=0$ for pure upwind and $\gamma=1$ for pure central; central differencing was implemented using a deferred correction technique for stability. Centred differences are used for diffusion terms. Temporal advancement is implicit, with pressure–velocity coupling through a modified PISO algorithm.[24] The k–ε equations are not implicitly coupled with the momentum, energy and pressure solutions, but are solved iteratively at the end of each time step.

To accommodate deformation of the computational mesh, an arbitrary Lagrangian–Eulerian (ALE) technique was adopted.[25] This permits the grid to move but does not by itself specify the motion of the grid points in response to boundary motion (piston and valves in our reciprocating-engine examples). Mesh integrity (minimal departures from orthogonality, positive Jacobians, etc.) is maintained by a mesh-deformation algorithm in which a field equation for grid-point velocities is solved with the prescribed boundary velocities as boundary conditions.[3]

At solid walls, fluid mean velocities are set to the boundary velocity $\mathbf{U}_b$. Standard wall-functions are used to set the level of the wall shear stress in the momentum equation and the dissipation rate in cells adjacent to the wall.[23] Normal stress terms (contributions from components normal to the boundary in the second term on the right-hand-side of equation (7)) were neglected in the momentum equations and hence in the computation of global balances. Stress terms on flow boundaries (i.e. the last term on right-hand-side of equation (10) at inflow/outflow boundaries) were neglected in the global balances.

All dependent variables are located at cell centres. Pressure forces in the momentum equation are treated by averaging the cell-centre pressures to obtain cell-face values; the treatment is such

that the pressure forces exerted on two elements sharing a common face differ if cell-face areas vary in the direction of the force. Thus, a component of linear momentum is a conserved quantity only in the case where the cell-face areas are uniform in the direction of interest. Angular momentum components, mean kinetic energy $\hat{K}$ and turbulence kinetic energy $\hat{k}$ are not conserved at the cell level.

First-order accurate time differences were used to compute the time–rate-of-change terms in the balances: in time-dependent flows, this results in an imbalance of order Δt (the computational time step) in the calculation of global balances for conserved variables. For non-conserved quantities, the imbalance remains non-zero and almost independent of time step for sufficiently small time steps. Linear momentum imbalance contributes to the imbalance in angular momentum. As argued earlier, imbalance in $\hat{K}$ is expected principally to reflect low-order spatial discretization errors and thus should be a good measure of numerical accuracy. Imbalance in $\hat{k}$ results in addition from the non-implicit nature of the k–ε solution and is less reliable as an indicator of discretization error.

5. APPLICATIONS

The utility of the balances is demonstrated through applications to flows in reciprocating engines. In the first example, the flow in an axisymmetric piston–cylinder assembly is computed; in the second, computations for a production four-valve-per-cylinder engine are reported. Various mesh densities and spatial differencing schemes were used in each case. The flows are complex, particularly for the production engine configuration, so that the benefits of the diagnostics for engineering flows will be amply demonstrated.

Axisymmetric piston–cylinder assembly

The axisymmetric piston–cylinder assembly is shown in Figure 1. Flow enters and leaves the cylinder through an annular port at an angle of 30° with respect to the cylinder axis. The piston is driven in simple harmonic motion at 200 rpm through a 60 mm stroke with a geometric compression ratio of 3:1. Laser-Doppler anemometry was used to extract radial profiles of mean and RMS axial velocity at several crank-angle positions during intake and compression.[26] This flow has been the subject of numerous modelling studies,[27–30] and the reader is referred to these studies for details of the flow and for comparisons between computations and measurements. Example comparisons between computed and measured mean axial velocities at 36° after top-dead-centre (TDC) are shown in Figure 2. It can be seen that agreement is good except at the second measurement station, where the computed profile undershoots the measured one.

Wedge-shaped computational meshes were used with the number of cells in the radial direction n_r equal to the number in the axial direction n_z and a single cell (5° wide) in azimuth. A non-uniform intake mean velocity profile was assumed, as shown in Figure 1(b). Meshes were uniform in z but non-uniform radially to accommodate the intake orifice (Figure 1(c)). A computational time step of 0·5 crank-angle degrees was used. With this value, results are independent of time step except as noted.

Local convergence is illustrated in Figure 3. There, the computed peak mean axial velocity at the measurement station closest to the head plane at 36° after TDC (Figure 2) has been plotted as a function of mesh spacing n_r and of differencing parameter γ. It can be seen that convergence is slow. By performing grid refinement tests with $\gamma = 0$ on 28×28 and 43×43 meshes, one might be inclined to interpret the small changes in computed profiles as near grid independence, while in fact the mean velocity has attained only about two-thirds of its converged value and convergence

is non-linear. While a formal Taylor series analysis for any $\gamma < 1$ shows that convergence should be linear in the mesh spacing, such an analysis is meaningful only in the limit as the mesh spacing approaches zero. A final point is that increasing the spatial accuracy of the convective differencing scheme is an effective approach to improved accuracy: an order-of-magnitude increase in the

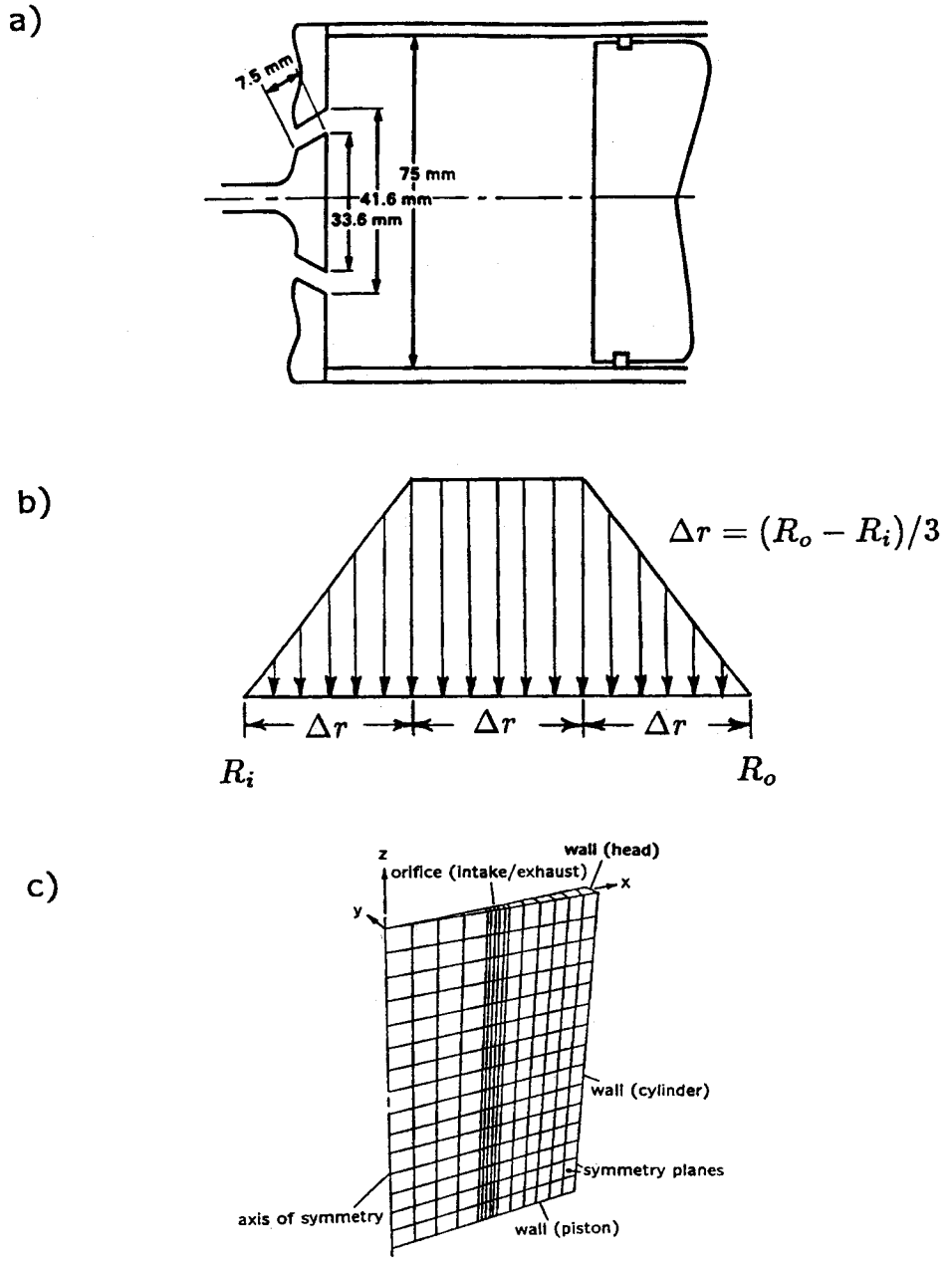

Figure 1. (a) Axisymmetric piston–cylinder assembly,[26] (b) intake mean axial velocity profile, (c) computational configuration ($n_r = n_z = 15$)

number of computational cells with $\gamma = 0$ gives the same improvement as increasing γ from 0·0 to 0·7 with $n_r = 28$. These results are typical of our experience with in-cylinder and other internal flows.

The evolution with crank angle θ of the global in-cylinder mean ($\hat{K}$, equation (14)) and turbulence ($\hat{k}$, equation (11)) kinetic energy is shown in Figure 4 for various n_r and γ. Both $\hat{K}$ and

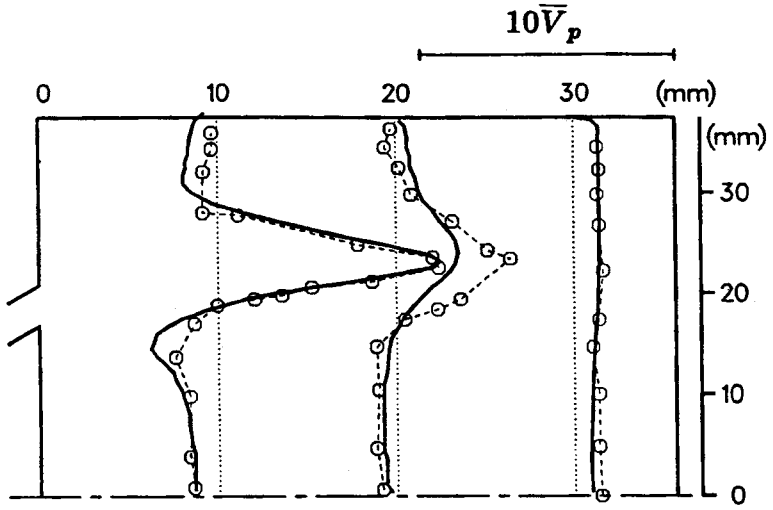

Figure 2. Computed (bold solid lines) and measured[26] (symbols, light dashed lines) mean axial velocity profiles at 36° after TDC normalized by the mean piston speed $\bar{V}_p = 0{\cdot}40$ m s^{-1}, axisymmetric configuration. Computations are for a 50 × 50 mesh with $\gamma = 0{\cdot}9$

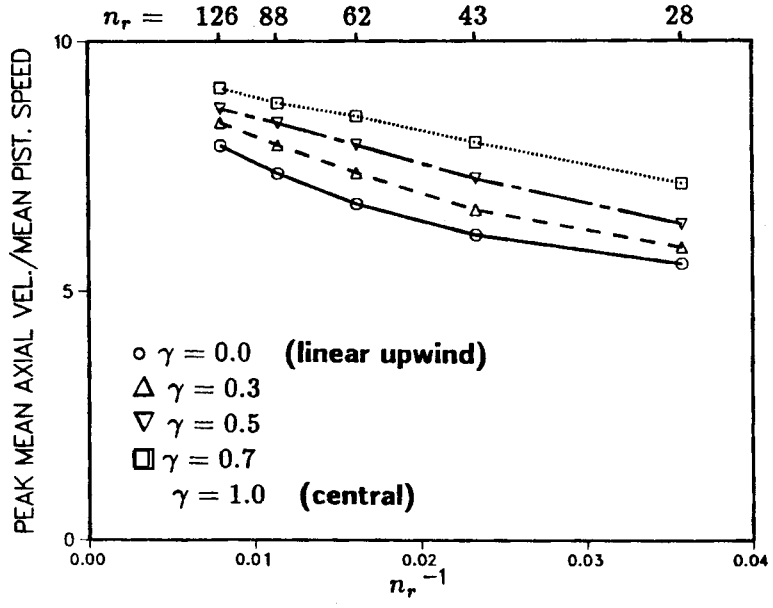

Figure 3. Peak mean axial velocity at $z = 10$ mm versus grid spacing n_r^{-1} and differencing scheme γ, axisymmetric configuration: (○) $\gamma = 0{\cdot}0$; (△) $\gamma = 0{\cdot}3$; (▽) $\gamma = 0{\cdot}5$; (□) $\gamma = 0{\cdot}7$

$\hat{k}$ increase with increasing spatial resolution and with higher-order differencing. This is consistent with the steeper mean velocity gradients that result from higher n_r and/or larger γ (Figure 3).

Mean kinetic energy balances are shown in Figure 5. The dominant term in equation (15) here is the pressure–velocity term PRES, which was split into contributions from the moving piston PRES_p and from the intake/exhaust orifice PRES_o: these two are almost equal and opposite. Four orders of magnitude smaller are the flux term FLUX, the imbalance IMBAL, the turbulence shear production PR1 and the time rate-of-change terms DMDT and D/DT; the remaining terms are negligible. It can be seen that IMBAL is negative in all cases, indicating a numerical loss of mean kinetic energy, as expected.

A single number that expresses the numerical loss of kinetic energy over the engine cycle is the normalized time integral $\overline{\text{IMBAL}}$ (equation (16)). This value is reported in Table I(b) along with

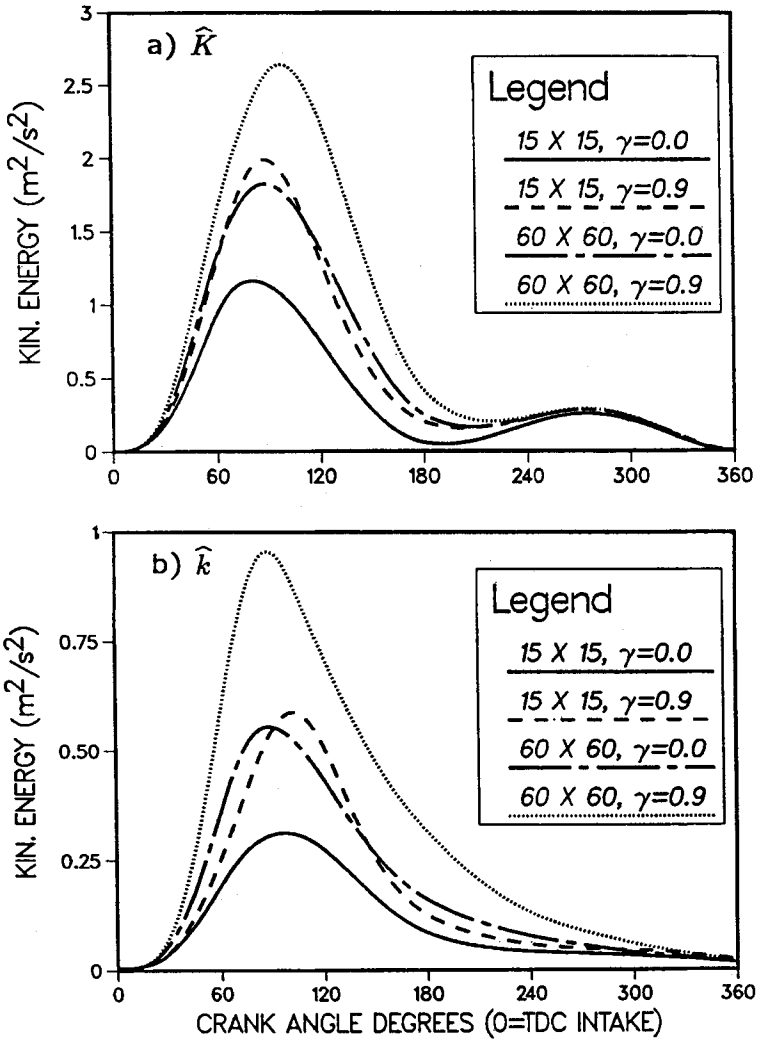

Figure 4. Evolution of global kinetic energy, axisymmetric configuration: (a) mean kinetic energy $\hat{K}$; (b) turbulence kinetic energy $\hat{k}$

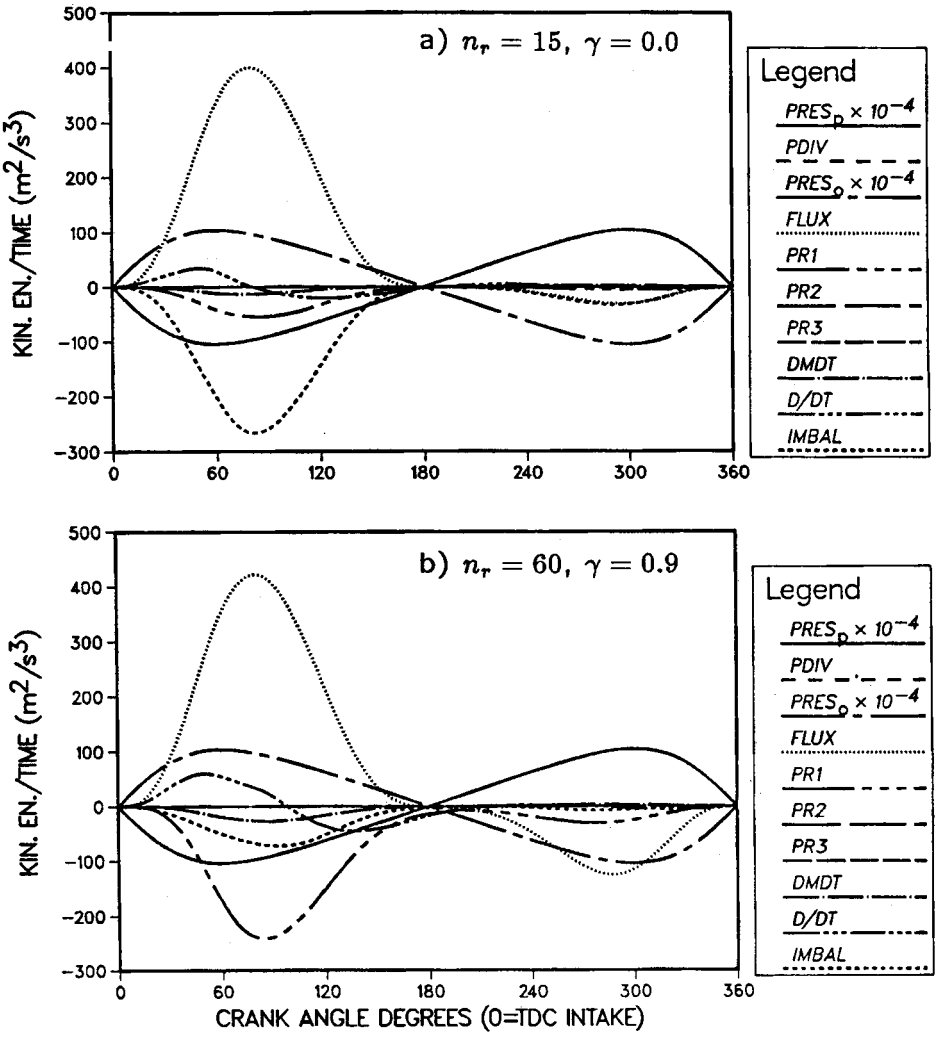

Figure 5. Mean kinetic energy balances, axisymmetric configuration: (a) $n_r = 15$, $\gamma = 0{\cdot}0$; (b) $n_r = 60$, $\gamma = 0{\cdot}9$

the normalized integrals of each of the other terms in equation (15). The magnitude of $\overline{\text{IMBAL}}$ decreases with increasing spatial resolution and with higher-order convective differencing, which suggests that indeed, imbalance in $\hat{K}$ is a useful indicator of low-order numerical errors. A normalized imbalance of unity ($\overline{\text{IMBAL}} = 1$) does not imply 100% error in $\hat{K}$ or in $d\hat{K}/dt$. It can be seen in Figures 4 and 5 that $d\hat{K}/dt$ does not absorb the entire decrease in $\overline{\text{IMBAL}}$ with improved numerical accuracy. Little further change in computed mean and RMS velocity profiles results with grid refinement beyond 60×60 with $\gamma = 0{\cdot}9$ ($\overline{\text{IMBAL}} \approx 1{\cdot}0$).

The only non-zero component of angular momentum is that about the y axis (Figure 1). The imbalance in this quantity is small in all cases ($\overline{\text{IMBAL}} < 0{\cdot}1$) and shows little response to grid refinement and spatial differencing (Table I(a)). Angular momentum imbalance in this example is probably dominated by the cell-face pressure imbalance in the radial direction. This and the order

Table I. Non-dimensionalized time-integrated (from 0° to 360°) terms in global balance equations for the axisymmetric piston-cylinder assembly (normalized as in equation (16)):

(a) y angular momentum (equation (13))

n_r	γ	$\overline{\text{FLUX}}$	$\overline{\text{PRES}_w}$	$\overline{\text{SHEAR}}$	$\overline{\text{PRES}_o}$	$\overline{\text{PRES}_s}$	$\overline{\text{IMBAL}}$
15	0·0	1·77	$6·15 \times 10^5$	0·035	$6·26 \times 10^5$	$1·16 \times 10^4$	0·085
30	0·0	1·81	$5·51 \times 10^5$	0·037	$5·61 \times 10^5$	$1·04 \times 10^4$	0·069
60	0·0	1·84	$4·99 \times 10^5$	0·062	$5·09 \times 10^5$	$9·47 \times 10^3$	0·082
15	0·9	1·75	$6·05 \times 10^5$	0·036	$6·16 \times 10^5$	$1·15 \times 10^4$	0·063
30	0·9	1·70	$5·22 \times 10^5$	0·057	$5·31 \times 10^5$	$9·88 \times 10^3$	0·072
60	0·9	1·62	$4·45 \times 10^5$	0·082	$4·53 \times 10^5$	$8·43 \times 10^3$	0·099

(b) Mean kinetic energy $\hat{K}$ (Equation (15))

n_r	γ	$\overline{\text{PRES}_p}$	$\overline{\text{PDIV}}$	$\overline{\text{PRES}_o}$	$\overline{\text{FLUX}}$	$\overline{\text{PR1}}$	$\overline{\text{PR2}}$	$\overline{\text{PR3}}$	$\overline{\text{DMDT}}$	$\overline{\text{IMBAL}}$
15	0·0	$6·92 \times 10^4$	0·0101	$6·92 \times 10^4$	10·16	1·47	$1·33 \times 10^{-3}$	$8·42 \times 10^{-6}$	0·36	6·94
30	0·0	$5·97 \times 10^4$	0·0114	$5·97 \times 10^4$	9·96	1·66	$1·59 \times 10^{-3}$	$1·30 \times 10^{-5}$	0·37	5·81
60	0·0	$4·88 \times 10^4$	0·0113	$4·88 \times 10^4$	9·10	2·52	$1·74 \times 10^{-3}$	$2·69 \times 10^{-5}$	0·38	3·93
15	0·9	$4·49 \times 10^4$	0·0055	$4·49 \times 10^4$	6·59	1·90	$1·02 \times 10^{-3}$	$6·03 \times 10^{-6}$	0·35	2·97
30	0·9	$3·80 \times 10^4$	0·0048	$3·80 \times 10^4$	6·29	2·48	$1·15 \times 10^{-3}$	$9·18 \times 10^{-6}$	0·37	1·92
60	0·9	$3·47 \times 10^4$	0·0062	$3·47 \times 10^4$	6·46	3·40	$1·36 \times 10^{-3}$	$2·03 \times 10^{-5}$	0·37	1·03

(c) Turbulence kinetic energy $\hat{k}$ (Equation (12))

n_r	γ	$\overline{\text{FLUX}}$	$\overline{\text{PR1}}$	$\overline{\text{PR2}}$	$\overline{\text{PR3}}$	$\overline{\text{DISS}}$	$\overline{\text{DMDT}}$	$\overline{\text{IMBAL}}$
15	0·0	2·11	6·68	$6·05 \times 10^{-3}$	$3·82 \times 10^{-5}$	5·17	0·42	2·32
30	0·0	2·16	7·59	$7·26 \times 10^{-3}$	$5·94 \times 10^{-5}$	6·49	0·40	1·44
60	0·0	2·17	9·00	$6·24 \times 10^{-3}$	$9·63 \times 10^{-5}$	7·54	0·40	0·79
15	0·9	1·15	7·01	$3·75 \times 10^{-3}$	$2·22 \times 10^{-5}$	4·89	0·35	2·40
30	0·9	1·29	8·55	$3·97 \times 10^{-3}$	$3·16 \times 10^{-5}$	6·65	0·37	1·69
60	0·9	1·42	9·85	$3·93 \times 10^{-3}$	$5·89 \times 10^{-5}$	8·16	0·38	1·02

Δt time differencing contribution can explain the insensitivity to n_r and γ. Pressure torques on walls (PRES_w), on the inlet orifice (PRES_o), and on the symmetry planes (PRES_s) sum nearly to zero.

The final budget is that for turbulence kinetic energy $\hat{k}$ (Figure 6, Table I(c)). The magnitude of each dominant term in the balance (FLUX, PR1, DISS), and more significantly, of the relative magnitude of the physical terms compared to the imbalance, increases with improved spatial resolution.

The results, shown in Figures 3–6 and Table I suggest that reasonably grid-independent results ($\overline{\text{IMBAL}} \leq 1$ in $\hat{K}$) for this relatively simple problem can be obtained with central differencing on a 60×60 grid; extrapolation implies that 240×240 may be required for comparable accuracy with standard upwind differencing. The global results are consistent with the local convergence results of Figure 3. Since CPU time is proportional to the number of computational elements while central differencing ($\gamma = 1$) increases computational time by just 15–20% compared to $\gamma = 0$, it is cost effective to invoke the higher-order spatial discretization scheme.

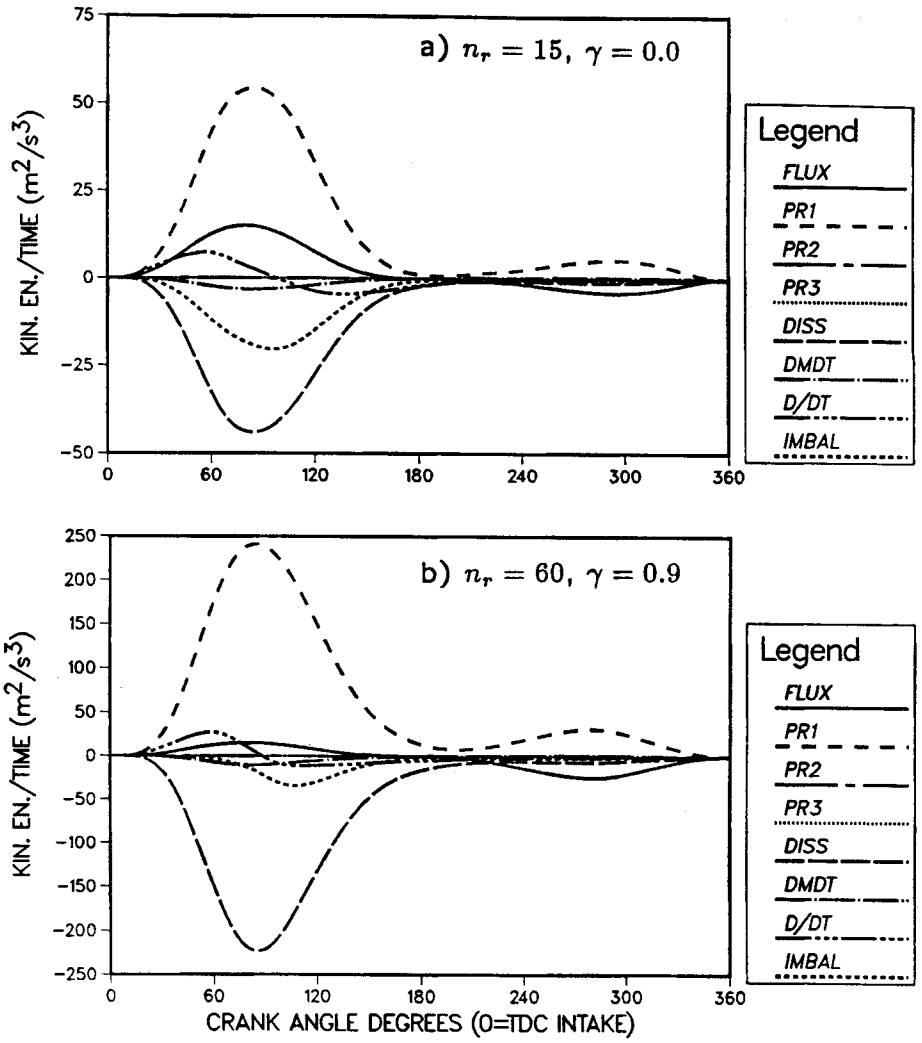

Figure 6. Turbulence kinetic energy balances, axisymmetric configuration: (a) $n_r = 15$, $\gamma = 0{\cdot}0$; (b) $n_r = 60$, $\gamma = 0{\cdot}9$

Production four-valve-per-cylinder engine

The second example is a production four-valve-per-cylinder engine (Figure 7). The operating conditions summarized in Table II were selected to match combustion experiments in this engine: one intake valve is inoperative, and the active valve has a reduced lift and is equipped with a 90° shroud that directs the flow entering the cylinder in the $+x$ direction.

Computations begin at intake-valve opening (IVO) and are carried to TDC compression. A pressure corresponding to the intake-manifold pressure is applied at the upstream end of the intake port and fresh charge is drawn into the cylinder as the valve opens and the piston moves downward. A variable computational time step is used, ranging from 1/16° at low valve lift to 1° through most of the calculation. Again, this was found to yield results that are reasonably time-step independent.

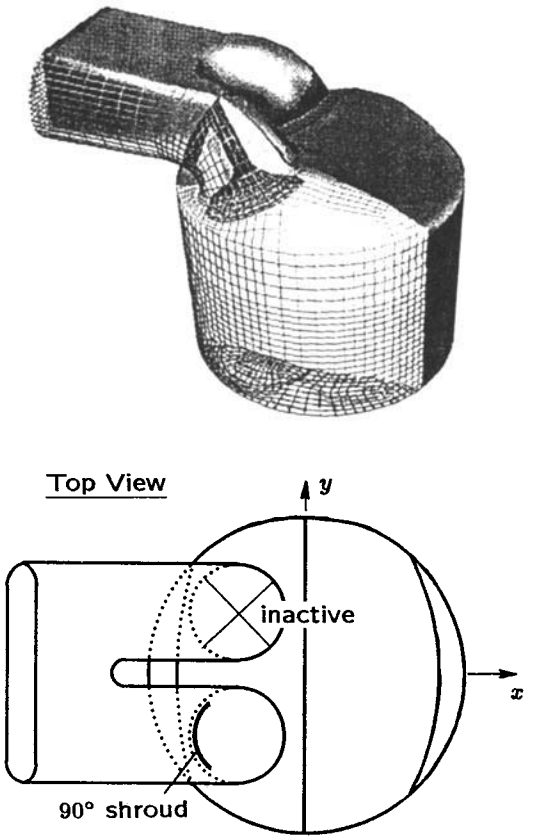

Figure 7. Production four-valve-per-cylinder port-and-cylinder mesh, with axis orientation: z axis coincides with cylinder axis

Global quantities of particular interest for in-cylinder flows include the in-cylinder 'swirl' (angular momentum about the cylinder axis) and 'tumble' (angular momentum about an axis normal to the cylinder axis), the mean kinetic energy $\hat{K}$ and the turbulence kinetic energy $\hat{k}$. In-cylinder turbulence levels at the time of ignition and burning (starting at about 30° before TDC compression) influence the flame propagation speed, and hence combustion performance. Mean kinetic energy is the 'reservoir' of energy available for turbulence generation, while swirl and tumble characterize the flow structure in which that energy is stored.

The global balances were performed in the in-cylinder subregion: thus the valve annulus (subscript f for 'flux boundary' in the following) forms one boundary of $V(t)$. Integrated imbalance terms are summarized in Table III, where n_c denotes the total number of cells. Separate results are given for IVO-to-540° and for IVO-to-720° to emphasize differences between intake and compression. Examples of angular momentum balances are shown in Figure 8. Influx of axial angular momentum through the valve annulus dominates the evolution of in-cylinder swirling angular momentum (D/DT tracks FLUX, Figure 8(c)); wall-pressure torque and influx are comparable for x tumble (Figure 8(a)) early on intake, while wall pressure dominates later, and wall pressure dominates throughout intake for y tumble (Figure 8(b)). There is a marked improvement in

Table II. Engine specifications and operating conditions

Bore	92·0 mm
Stroke	85·0 mm
Connecting rod	147·5 mm
Compression ratio	9·3:1
IVO	379° after TDC (lift = 0·35 mm)
IVC	565° after TDC (lift = 0·35 mm)
Max valve lift	5·57 mm at 471° after TDC
Valve shroud	90°, facing $+x$ (Figure 7)
Engine speed	1300 rpm
Manifold pressure	62 kPa
Manifold temperature	378 K
IVO in-cylinder pressure	73 kPa
IVO in-cylinder temperature	778 K

Table III. Non-dimensionalized time-integrated (from IVO to θ) imbalance terms for the production four-valve-per-cylinder engine [normalized as in equation (16)]

n_c	γ	θ	$\overline{\text{IMBAL}}_{\text{ang } x}$	$\overline{\text{IMBAL}}_{\text{ang } y}$	$\overline{\text{IMBAL}}_{\text{ang } z}$	$\overline{\text{IMBAL}}_{\hat{K}}$	$\overline{\text{IMBAL}}_{\hat{\varepsilon}}$
22 920	0·0	540°	0·31	1·05	0·74	7·86	14·10
39 780	0·0	540°	0·25	0·86	0·67	7·43	10·40
65 383	0·0	540°	0·19	0·58	0·55	6·72	6·44
39 780	0·9	540°	0·16	0·56	0·28	4·86	7·74
39 780	1·0	540°	0·15	0·56	0·16	3·40	7·86
22 920	0·0	720°	0·28	0·82	0·72	7·48	13·61
39 780	0·0	720°	0·21	0·64	0·63	6·81	8·73
39 780	0·9	720°	0·12	0·38	0·30	4·63	7·57

angular momentum imbalance with grid refinement and with higher-order convective differencing (Table III).

Mean kinetic energy balances (Figure 9) again reveal the dominance of pressure–work terms; the pressure-divergence term becomes important during compression. Imbalance decreases both with n_c and with γ (Table III). As before, higher-order numerics is a more cost-effective route to improved accuracy than grid refinement. Even for the best case reported in Table III, $\overline{\text{IMBAL}}_K = 3{\cdot}4$, indicating that results are not yet grid independent. Turbulence kinetic energy balances are shown in Figure 10. For the first-order upwind scheme, numerical dissipation ($\overline{\text{IMBAL}}$) is comparable in magnitude to the viscous dissipation (Table III). The relative magnitude of the imbalance improves with spatial resolution and with differencing, although it remains large even for the best case shown. The explicit k–ε treatment probably contributes to the large imbalance.

Computed peak energies and bottom–dead-centre (BDC) energies and angular momentum are summarized in Table IV. The strong influence of numerics on these important global quantities is clear. Differences among computed values of $\hat{K}$ and $\hat{\varepsilon}$ diminish during compression (see also Figure 4): higher $\hat{K}$ yields higher turbulence production which acts to reduce $\hat{K}$, and higher $\hat{\varepsilon}$ is associated with higher turbulence dissipation rates. While increasing the number of computational elements by a factor of three results in relatively little improvement in computed swirl,

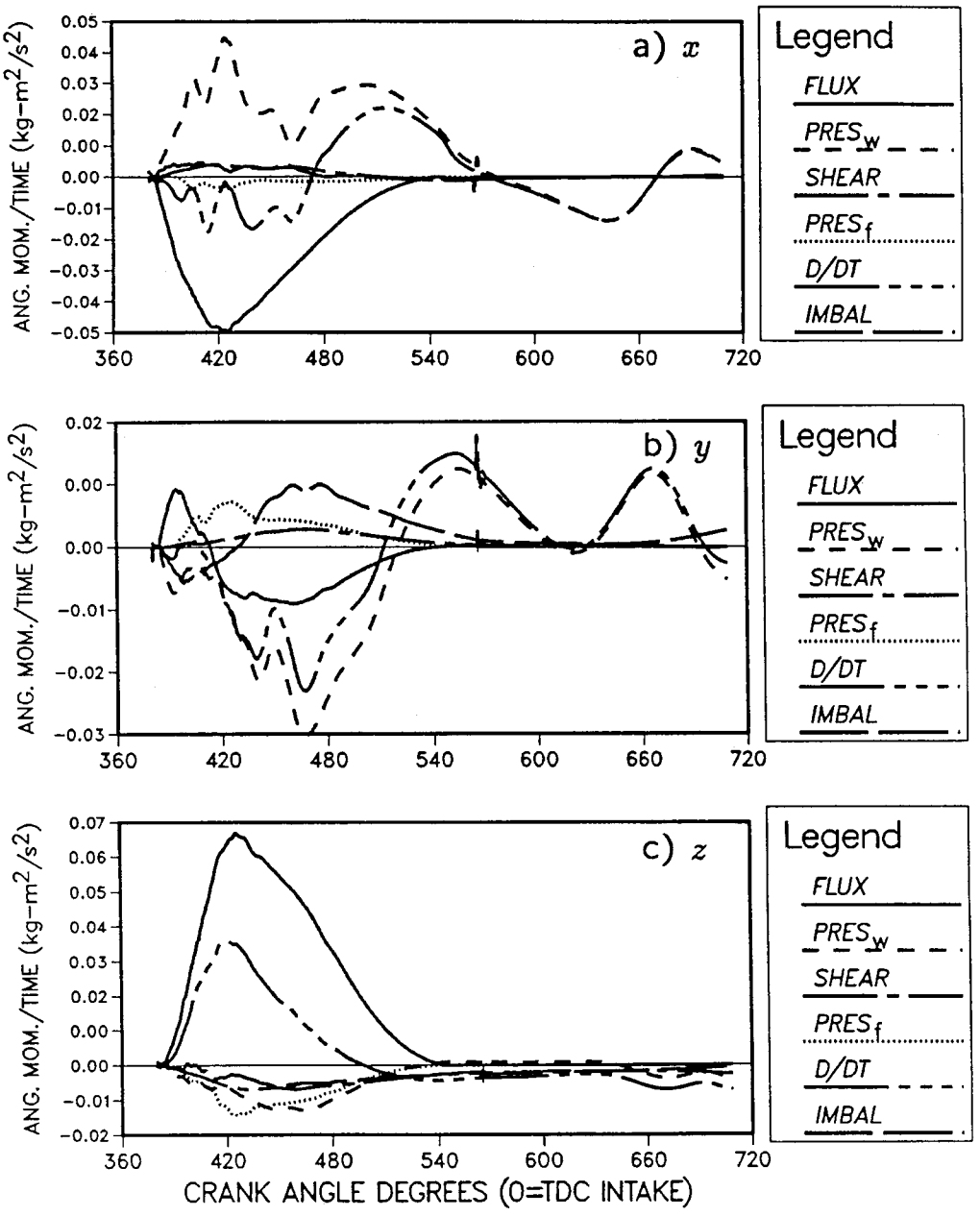

Figure 8. Angular momentum balances, production configuration, $n_c = 39\,780$, $\gamma = 0{\cdot}9$: (a) x; (b) y; (c) z

improved spatial differencing yields significant improvement. The measured BDC swirl ratio (determined from steady-flow measurements and a zero-dimensional engine simulation)[31] ranges from 5·0 to 6·6.

Figures 8–10 and Tables III and IV amply illustrate the well-known deficiencies of standard upwind differencing. Some 500 000 cells with upwind would be needed to reduce $\overline{\text{IMBAL}}$ to the

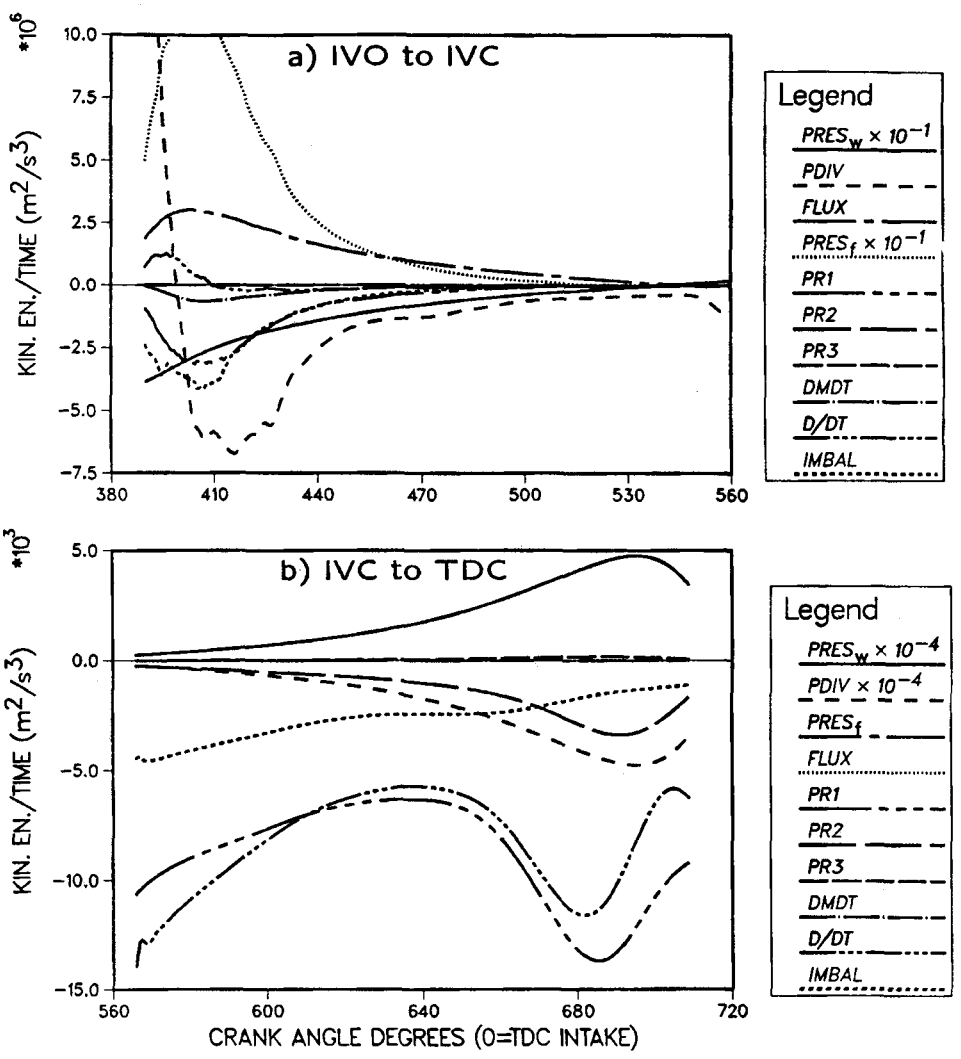

Figure 9. Mean kinetic energy balances, production configuration, $n_c = 39\,780$, $\gamma = 0{\cdot}9$: (a) IVO–IVC; (b) IVC–710°

level achieved using 40 000 cells with central differencing. Even for central differencing, results are not fully grid-independent on the 40 000-cell mesh. A practical upper limit for time-dependent three-dimensional in-cylinder computations at present is about 250 000 ($\approx 65^3$) cells.

We conclude with an illustration of the physical insight that can be gained using the balances. Because induction-generated turbulence has largely dissipated by IVC (Figure 10),[3] the bulk fluid motion is important for its potential to generate additional turbulence close to TDC, thereby enhancing the burn rate. In References 1 and 3, global balances were employed to elucidate a mechanism for turbulence production through the breakdown of large-scale motions. Briefly, it was found that tumble is more effective than swirl in generating late-compression turbulence. Tumble more efficiently extracts energy from the piston motion during compression. This is reflected in the 'spin-up' in the x and y components of angular momentum after 600°, while

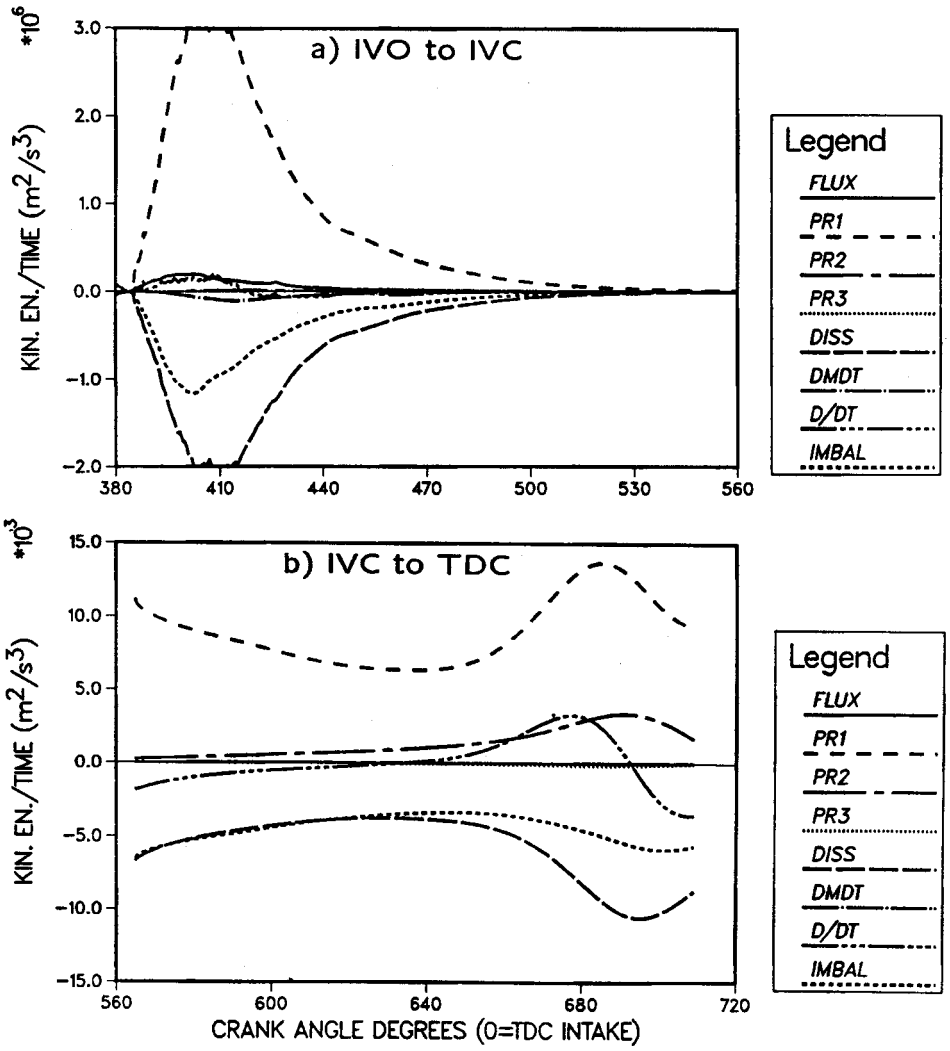

Figure 10. Turbulence kinetic energy balances, production configuration, $n_c = 39\,780$, $\gamma = 0{\cdot}9$: (a) IVO–IVC; (b) IVC–710°

Table IV. Peak and BDC mean and turbulence kinetic energy, and BDC swirl ratio SR_z and tumble ratios TR_x and TR_y for the production configuration. Peaks occur near 420° after TDC in all cases. Swirl and tumble ratios are the angular momentum about the specified axis, divided by the fluid moment of inertia about that axis, and normalized by the crankshaft angular speed

n_c	γ	$\hat{K}_{peak}$	$\hat{K}_{peak}$	$\hat{K}_{BDC}$	$\hat{k}_{BDC}$	TR_x	TR_y	SR_z
22 290	0·0	1402	98·2	182·3	8·49	0·75	1·70	3·61
39 780	0·0	1474	128·0	201·0	12·2	0·77	1·83	3·75
65 383	0·0	1550	201·0	236·3	23·3	0·93	1·96	4·05
39 780	0·9	2232	399·0	339·3	28·0	0·70	2·30	4·89
39 780	1·0	2293	480·0	355·1	32·0	0·75	2·29	5·03

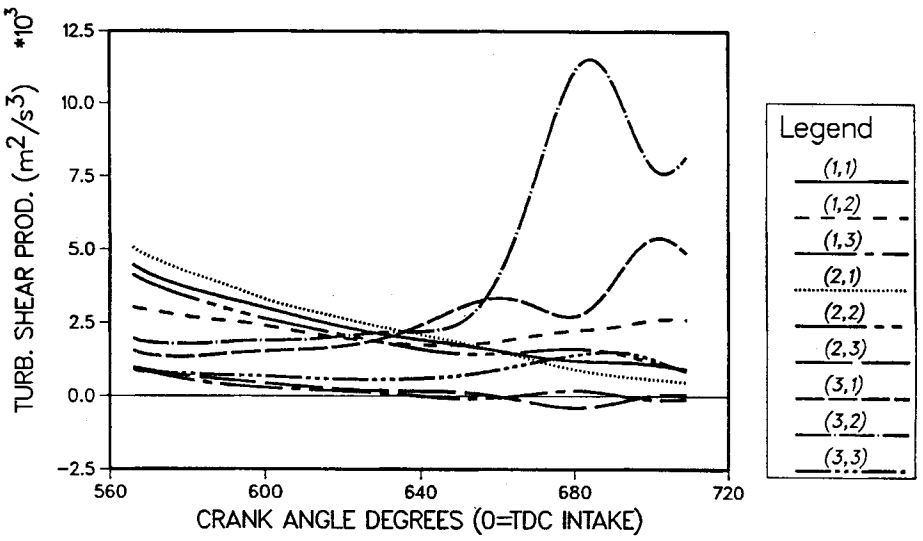

Figure11. Volume-integrated components of turbulence shear production (nine (i, j) contributions summed to yield $P1_{pk}$ in Equation (9)) versus crank angle, production configuration, $n_c = 39\,780$, $\gamma = 0{\cdot}9$: $1 = x$; $2 = y$; $3 = z$

swirl simply decays (Figure 8); the rate-of-decrease of mean kinetic energy is small at this time (Figure 9(b)). As the in-cylinder aspect ratio (height-to-bore) continues to decrease, a single cylinder-filling tumble vortex no longer 'fits' and small-scale turbulence is generated as the tumble breaks down. This can be seen in the later drop in x and y angular momentum (Figure 8), the simultaneous large negative $d\hat{K}/dt$ (Figure 9(b)), and positive $d\hat{k}/dt$ from 640° to 690° with large PR1 (Figure 10(b)). Further evidence supporting the contention that it is tumble, and not swirl, that is responsible for this pre-TDC turbulence is given in Figure 11. There the volume integral of each of the nine (i, j) components that are summed to yield the total turbulence shear production ($P1_{pk}$ in equation (9)) has been plotted. The dominant terms late during compression are (3, 1)=(z, x) and (3, 2)=(z, y): these correspond to velocity gradients representing rotations about the 2(y) and 1 (x) axes, respectively.

6. DISCUSSION

It has been demonstrated that imbalances in quantities not conserved at the cell level can be used as indicators of numerical accuracy in complex time-dependent internal flow problems. By comparing the magnitude of the imbalance to physical terms in the balance equations, the relative influence of discretization error compared to physical processes is revealed directly. For specific numerical schemes (e.g. upwind differencing of the convective operator), the energy-dissipating character of the truncation error suggests that the imbalance in mean kinetic energy should be particularly useful as a measure of low-order spatial discretization errors.

For other numerical schemes and other physical quantities, the imbalances approach zero in the limit of a converged solution. Monotonic convergence of the imbalances in angular momentum and turbulence kinetic energy with improving spatial accuracy has been found in all flows examined to date, provided that time-stepping error and cell-face pressure imbalances are sufficiently small. The magnitude of the imbalance terms decreases with increasing mesh density and with the implementation of higher-accuracy spatial discretization schemes. By contrast to

grid refinement, this approach allows a direct assessment of numerical accuracy in a single-computational run using a single mesh. Although the present approach is not expected to capture all manifestations of numerical inaccuracy, it does provide useful guidance for the modeller in determining to what extent results may be tainted by numerical error.

Balances can be applied over the entire solution domain or over subdomains down to the individual cell level. The present examples were limited to large subdomains. In applications, we routinely divide the computational domain into several subdomains (e.g. intake ports, in-cylinder, exhaust ports) based on the physical information sought.

The examples presented here were limited to blends of upwind and central differencing because these are the schemes that are available in the unstructured hex-mesh code employed for this study. Although results are markedly improved with the second-order scheme, second-order differencing is not a panacea to the numerical accuracy issue. The balances suggest that numerical accuracy remains marginal, at best, for the second example problem (practical port-and-cylinder configuration) even with central differencing. Moreover, the reduced stability of the central-differencing scheme makes it less attractive for 'production' CFD applications. Higher-order methods such as the third-order upwind scheme used in the in-cylinder computations of Reference 20 may yield further improvements. There remains a strong incentive for continuing research into improved discretization schemes to address the often conflicting requirements of accuracy, robustness and geometric flexibility.

In addition to numerical accuracy information, the relative magnitude of each term in the balances provides insight into the physical processes occurring in the volume of integration. The utility of this aspect of the balances has been illustrated through application to a production four-valve-per-cylinder engine: differences between swirl and tumble have been pointed out both in their generation and in their capacity to generate turbulence.

To improve further the utility of multidimensional modelling, research into advanced sub-models for turbulence, turbulent combustion and fuel sprays is in progress. Numerical error estimation and control are prerequisites to the successful implementation and application of these models. The strong influence of numerics on computed angular momentum $\hat{K}$ and $\hat{k}$ has been demonstrated. Species mixing, turbulent combustion and spray models all require turbulence intensity and scales as input. Attempts to calibrate or apply these models without understanding and controlling numerical errors will hinder progress in advanced modelling.

It is likely that a combination of local and global error estimates will prove most viable as a strategy for automated error estimation and correction (e.g. via adaptive grid refinement). Work is ongoing to relate cell-level imbalances with other local error estimates, to further correlate local imbalances with global imbalances, and to devise adaptive meshing strategies based on these imbalances.

ACKNOWLEDGEMENTS

The authors thank Dr. Shengming Chang (GMR Engine Research Department) for valuable discussions on numerical implementation of balances and Dr. Ping-Ho Tsai (GMR Thermosciences Department) for the computational results shown in Figure 2.

APPENDIX

In this appendix derivations of global balance equations are sketched. Briefly, the balance for any quantity $\Phi = \Phi(x, t)$ (scalar or vector component) is derived by integrating the partial differential equation governing Φ over the time-dependent volume of interest $V(t)$ and manipulating the

result into a convenient form. The manipulations are principally of two types: first, the divergence theorem is invoked to convert volume integrals into integrals over the bounding surface $S(t)$, and second, the equation relating integrals of time derivatives to the time derivative of the integral and a contribution from the moving boundaries is used,

$$\int_{V(t)} \frac{\partial \Phi_i}{\partial x_i} \, d\tau = \int_{S(t)} \Phi_i \, dA_i, \quad \int_{V(t)} \frac{\partial \Phi}{\partial t} \, d\tau = \frac{d}{dt} \int_{V(t)} \Phi \, d\tau - \int_{S(t)} \Phi V_{Bi} \, dA_i \tag{4}$$

In equation (4), $d\tau$ represents a volume element of $V(t)$ and dA_i is the ith component of the outward-pointing surface-element vector; V_{Bi} is the ith component of the boundary velocity.

Governing partial differential equations

The set of equations considered is the compressible continuity and momentum equations together with a two-equation k–ε turbulence model. The approach applies equally well to any other set of partial differential equations. We use (without loss of generality) the ensemble-averaged form of the equations: angled brackets $\langle \ \rangle$ denote conventional (volume) averages while a tilde is used for density-weighted (Favre) averages. A double prime denotes a fluctuation with respect to a Favre mean quantity. Fluid density, pressure, velocity and viscosity are denoted by ρ, p, U and μ, respectively; k and ε are the turbulence kinetic energy and its dissipation rate. Details can be found in Reference 3.

The ensemble-averaged continuity and momentum equations are

$$\frac{\partial \langle \rho \rangle}{\partial t} + \frac{\partial \langle \rho \rangle \tilde{U}_i}{\partial x_i} = 0, \tag{5}$$

$$\frac{\partial \langle \rho \rangle \tilde{U}_i}{\partial t} + \frac{\partial \langle \rho \rangle \tilde{U}_i \tilde{U}_j}{\partial x_j} = -\frac{\partial \langle p \rangle}{\partial x_i} + \frac{\partial \tilde{\tau}_{\text{eff}\,ji}}{\partial x_j}. \tag{6}$$

In equation (6), the effective stress $\tilde{\tau}_{\text{eff}\,ji}$ is the sum of a turbulent stress or Reynolds stress $\tau_{t\,ji}$ and the mean viscous stress, $\tilde{\tau}_{\text{eff}\,ji} = \tilde{\tau}_{t\,ji} + \langle \tau_{ji} \rangle$. The turbulent stress is treated using a standard two-equation k–ε turbulence model,[23]

$$\tilde{\tau}_{t\,ji} = -\frac{2}{3}\langle \rho \rangle k \delta_{ji} + \mu_t \left(\frac{\partial \tilde{U}_j}{\partial x_i} + \frac{\partial \tilde{U}_i}{\partial x_j} \right) - \frac{2}{3}\mu_t \frac{\partial \tilde{U}_l}{\partial x_l} \delta_{ji}, \quad \mu_t = C_\mu \langle \rho \rangle k^2/\varepsilon, \tag{7}$$

where $k = \widetilde{u_i'' u_i''}/2$ is the turbulence kinetic energy, μ_t is the turbulent viscosity and C_μ is a model constant. To complete the model, equations governing the evolution of k and ε are needed. Here we are concerned primarily with the k equation,

$$\frac{\partial \langle \rho \rangle k}{\partial t} + \frac{\partial \langle \rho \rangle \tilde{U}_j k}{\partial x_j} = \frac{\partial}{\partial x_j} \left(\frac{\mu_{\text{eff}}}{\sigma_k} \frac{\partial k}{\partial x_j} \right) + \tilde{\tau}_{t\,ji} \frac{\partial \tilde{U}_j}{\partial x_i} - \langle \rho \rangle \varepsilon, \tag{8}$$

where $\mu_{\text{eff}} = \mu_t + \mu$. The dissipation equation and values of all model constants are those suggested by El Tahry[23] for modelling studies of in-cylinder flows.

In equation (8), the penultimate term represents the production of turbulence kinetic energy by interaction of the turbulent velocity fluctuations with mean velocity gradients. It is useful to

expand this term into three parts using equation (7),

$$P_{\rho k} \equiv \tilde{\tau}_{t\,ji} \frac{\partial \tilde{U}_j}{\partial x_i} = \mu_t \left(\frac{\partial \tilde{U}_j}{\partial x_i} + \frac{\partial \tilde{U}_i}{\partial x_j} \right) \frac{\partial \tilde{U}_j}{\partial x_i} - \frac{2}{3} \langle \rho \rangle k \frac{\partial \tilde{U}_j}{\partial x_j} - \frac{2}{3} \mu_t \frac{\partial \tilde{U}_j}{\partial x_j} \frac{\partial \tilde{U}_l}{\partial x_l}$$

$$= \quad P1_{\rho k} \quad + \quad P2_{\rho k} + \quad P3_{\rho k}. \tag{9}$$

Global balance equations

The procedure outlined above is applied to equation (6) to yield the global balance of mean linear momentum ($\Phi = \langle \rho \rangle \tilde{U}_i$ is the mean linear momentum per unit volume),

$$0 = \frac{\mathrm{d}}{\mathrm{d}t} \int_{V(t)} \langle \rho \rangle \tilde{U}_i \, \mathrm{d}\tau + \int_{S(t)} \langle \rho \rangle \tilde{U}_i \tilde{U}_{\mathrm{rel}\,j} \, \mathrm{d}A_j + \int_{S(t)} \langle \rho \rangle \, \mathrm{d}A_i - \int_{S(t)} \tilde{\tau}_{\mathrm{eff}\,ji} \, \mathrm{d}A_j$$

$$\mathrm{IMBAL} = \mathrm{D/DT} - \mathrm{FLUX} - \mathrm{PRES} - \mathrm{SHEAR}. \tag{10}$$

Here $\tilde{U}_{\mathrm{rel}\,j}$ represents the *jth* component of the mean fluid velocity relative to the boundary, $\tilde{U}_{\mathrm{rel}\,j} = \tilde{U}_j - V_{Bj}$. The names assigned on the second line of equation (10) are used to distinguish the various contributions in the presentation of results (Section 5). IMBAL is the global imbalance in a numerical computation of equation (10).

A global mass-averaged turbulence kinetic energy $\hat{k}$ is defined as

$$\hat{k} \equiv \frac{1}{m} \int_{V(t)} \langle \rho \rangle \, k \, \mathrm{d}\tau, \tag{11}$$

where m is the total fluid mass in $V(t)$, $m \equiv \int_{V(t)} \langle \rho \rangle \, \mathrm{d}\tau$. The equation governing $\hat{k}$ is derived by integrating and manipulating equation (8),

$$0 = \frac{\mathrm{d}\hat{k}}{\mathrm{d}t} + \frac{1}{m} \int_{S(t)} \langle \rho \rangle \, k \tilde{U}_{\mathrm{rel}\,j} \, \mathrm{d}A_j - \frac{1}{m} \int_{S(t)} \frac{\mu_{\mathrm{eff}}}{\sigma_k} \frac{\partial k}{\partial x_j} \, \mathrm{d}A_j - \frac{1}{m} \int_{V(t)} P1_{\rho k} \, \mathrm{d}\tau$$

$$- \frac{1}{m} \int_{V(t)} P2_{\rho k} \, \mathrm{d}\tau - \frac{1}{m} \int_{V(t)} P3_{\rho k} \, \mathrm{d}\tau + \frac{1}{m} \int_{V(t)} \langle \rho \rangle \, \varepsilon \, \mathrm{d}\tau + \frac{1}{m} \frac{\mathrm{d}m}{\mathrm{d}t} \hat{k}$$

$$\mathrm{IMBAL} = \mathrm{D/DT} - \mathrm{FLUX} - \mathrm{SHEAR} - \mathrm{PR1} - \mathrm{PR2} - \mathrm{PR3} - \mathrm{DISS} - \mathrm{DMDT}. \tag{12}$$

Global balance equations for derived quantities can also be found. Two quantities of particular interest for physical and numerical diagnostics are the angular momentum and the mean kinetic energy, respectively. The *kth* component of mean angular momentum of a fluid volume element $\mathrm{d}\tau$ about a point Q is given by $\mathrm{d}H_k = \langle \rho \rangle \, \varepsilon_{ijk} \phi_i \tilde{U}_j \, \mathrm{d}\tau$, where $\mathbf{r}$ is a position vector from origin Q and ε_{ijk} is the alternating tensor. The global mean angular momentum balance results from taking $r \times$ equation (6) and integrating

$$0 = \frac{\mathrm{d}}{\mathrm{d}t} \int_{V(t)} \langle \rho \rangle \, \varepsilon_{ijk} r_i \tilde{U}_j \mathrm{d}\tau + \int_{S(t)} \langle \rho \rangle \, \varepsilon_{ijk} r_i \tilde{U}_j \tilde{U}_{\mathrm{rel}\,l} \, \mathrm{d}A_l + \int_{S(t)} \langle p \rangle \, \varepsilon_{ijk} r_i \, \mathrm{d}A_j - \int_{S(t)} \varepsilon_{ijk} r_i \tilde{\tau}_{\mathrm{eff}\,lj} \, \mathrm{d}A_l$$

$$\mathrm{IMBAL} = \mathrm{D/DT} - \mathrm{FLUX} - \mathrm{PRES} - \mathrm{SHEAR}. \tag{13}$$

The final balance is that for global mean kinetic energy $\hat{K}$,

$$\hat{K} \equiv \frac{1}{m} \int_{V(t)} \frac{1}{2} \langle \rho \rangle \tilde{U}_j \tilde{U}_j \, \mathrm{d}\tau. \tag{14}$$

The equation governing $\hat{K}$ is derived by taking the inner product of $\tilde{\mathbf{U}}$ with equation (6), integrating over the volume $V(t)$ and manipulating the result,

$$0=\frac{\mathrm{d}\hat{K}}{\mathrm{d}t}+\frac{1}{m}\int_{S(t)}\frac{1}{2}\langle\rho\rangle\tilde{U}_j\tilde{U}_j\tilde{U}_{\mathrm{rel}\,l}\,\mathrm{d}A_l+\frac{1}{m}\int_{S(t)}\langle p\rangle\tilde{U}_j\,\mathrm{d}A_j-\frac{1}{m}\int_{V(t)}\langle p\rangle\frac{\partial\tilde{U}_j}{\partial x_j}\mathrm{d}\tau+\frac{1}{m}\int_{V(t)}P1_{\rho k}\,\mathrm{d}\tau$$
$$+\frac{1}{m}\int_{V(t)}P2_{\rho k}\,\mathrm{d}\tau+\frac{1}{m}\int_{V(t)}P3_{\rho k}\,\mathrm{d}\tau-\frac{1}{m}\int_{S(t)}\tilde{\tau}_{\mathrm{eff}\,ji}\tilde{U}_j\;\mathrm{d}A_i+\frac{1}{m}\frac{\mathrm{d}m}{\mathrm{d}t}\hat{K}$$
$$\mathrm{IMBAL}=\mathrm{D/DT}-\mathrm{FLUX}-\mathrm{PRES}-\mathrm{PDIV}-\mathrm{PR1}-\mathrm{PR2}-\mathrm{PR3}-\mathrm{SHEAR}-\mathrm{DMDT}. \quad (15)$$

Higher moments such as $\hat{K}$ are expected to be sensitive indicators of numerical accuracy.

A convenient single-number representation of the contribution of each physical process and of numerical accuracy is the normalized time integral of the absolute value of the corresponding term in the global balance equation. For equation (10), for example,

$$\overline{\mathrm{IMBAL}}=\int_0^t|\mathrm{IMBAL}|\,\mathrm{d}t'\Big/\int_0^t|\mathrm{D/DT}|\mathrm{d}t',\quad \overline{\mathrm{D/DT}}=\int_0^t|\mathrm{D/DT}|\,\mathrm{d}t'\Big/\int_0^t|\mathrm{D/DT}|\,\mathrm{d}t',$$

$$\overline{\mathrm{FLUX}}=\int_0^t|\mathrm{FLUX}|\,\mathrm{d}t'\Big/\int_0^t|\mathrm{D/DT}|\,\mathrm{d}t',\quad \overline{\mathrm{PRES}}=\int_0^t|\mathrm{PRES}|\,\mathrm{d}t'\Big/\int_0^t|\mathrm{D/DT}|\,\mathrm{d}t',$$
$$\overline{\mathrm{SHEAR}}=\int_0^t|\mathrm{SHEAR}|\,\mathrm{d}t'\Big/\int_0^t|\mathrm{D/DT}|\,\mathrm{d}t', \quad (16)$$

and similarly for equations (12), (13) and (15). Each term in equation (16) represents the magnitude of that term relative to the time-rate-of-change. Clearly $\overline{\mathrm{D/DT}}\equiv 1$. Further discussion of these balances can be found in Section 5 of this paper and in Reference 3.

REFERENCES

1. A. D. Gosman, Y. Y. Tsui and C. Vafidis, 'Flow in a model engine with a shrouded valve—a combined experimental and computational study', *SAE Paper 85-0498*, 1985.
2. T.-W. Kuo and R. D. Reitz, 'Computation of premixed-charge combustion in pancake and pent-roof engines', *SAE Paper 89-0670*, 1989.
3. D. C. Haworth, S. H. El Tahry, M. S. Huebler and S. Chang, 'Multidimensional port-and-cylinder flow calculations for two- and four-valve-per-cylinder engines: influence of intake configuration on flow structure', *SAE Paper 90-0255*, 1990.
4. J. D. Naber and R. D. Reitz, 'Modeling spray/wall interactions in engines', *SAE Paper 88-0107*, 1988.
5. J. Abraham and F. V. Bracco, 'Comparisons of computed and measured pressures in a premixed-charge natural gas fueled rotary engine', *SAE Paper 89-0671*, 1989.
6. B. Smith, 'Application of turbulence modeling to the design of military aircraft', *AIAA Paper 91-0513*, 1991.
7. O. Sharma and S. Syed, 'Turbulence modeling use in gas turbine design/analysis', *AIAA Paper 91-0514*, 1991.
8. S. H. El Tahry and D. C. Haworth, 'Directions in turbulence modeling for in-cylinder flows in reciprocating engines', *AIAA J. Prop. Power*, **8**, 1040–1048 (1992).
9. P. J. Roache, *Computational Fluid Dynamics*, Hermosa, Albuquerque, 1976.
10. R. Vichnevetsky and J. B. Bowles, 'Fourier analysis of numerical approximations of hyperbolic equations,' *SIAM Studies Appl. Math.*, **5**, (1982).
11. T. J. R. Hughes and T. Shakib, 'Computational aerodynamics and the finite element method', *AIAA Paper 88-0031*, 1988.
12. M. J. Andrews and F. V. Bracco, 'The use of intake and exhaust measurements with computer simulations to investigate the evolution of the internal flowfield in a ported engine', *SAE Paper 91-0262*, 1991.
13. L. Hesselink, 'Digital image processing in flow visualization', *Ann. Rev. Fluid Mech.*, **20**, 421–485 (1988).
14. P. P. Walatka and P. G. Buning, 'PLOT3D' user's manual, *NASA Tech. Memo.*, 1989.
15. J. Helman and L. Hesselink, 'Representation and display of vector field topology in fluid flow data sets', *IEEE Comput. Magazine*, **8**, 27–36 (1989).

16. M. Chong, A. Perry and B. Cantwell, 'A general classification of three-dimensional flow fields', *Phys. Fluids*, **A2**, 765–777 (1990).
17. H. Tennekes and J. L. Lumley, *A First Course in Turbulence*, MIT Press, Cambridge, MA, 1972.
18. M. S. Anand and S. B. Pope, 'Calculations of premixed turbulent flames by pdf methods', *Combust. Flame*, **67**, 127–142 (1987).
19. P. J. O'Rourke, 'The Turn function and vorticity method for numerical fluid dynamics', *J. Comput. Phys.*, **53**, 359–381 (1984).
20. K. Naitoh, H. Jujii, T. Urushihara, Y. Takagi and K. Kuwahara, 'A computational model for the detailed flows in the ports and cylinder of reciprocating engine', *SAE Paper 900256*, 1990.
21. E. S. Oran and J. P. Boris, *Numerical Simulation of Reactive Flow*, Elsevier, New York, 1987.
22. I. Demirdzic, A. D. Gosman, R. I. Issa and M. Peric, 'A calculation procedure for turbulent flow in complex geometrics', *Comput. Fluids*, **15**, 251–273 (1987).
23. S. H. El Tahry, 'k–ε equations for compressible reciprocating engine flows', *J. Energy*, **7**, 345–353 (1983).
24. R. I. Issa, 'Solution of the implicitly discretized fluid flow equations by splitting of operators', *J. Comput. Phys.*, **62**, 40–65 (1986).
25. C. W. Hirt, A. A. Amsden and J. L. Cook, 'An arbitrary Lagrangian–Eulerian computing method for all flow speeds', *J. Comput. Phys.*, **14**, 227–253 (1974).
26. C. Vafidis and J. H. Whitelaw, 'Intake valve and in-cylinder flow development in a reciprocating model engine', *Report FS/84/32*, Imperial College Department Mechanical Engineering, London, U.K., 1984.
27. A. D. Gosman, R. J. R. Johns and A. P. Watkins, 'Development of prediction methods for in-cylinder processes in reciprocating engines', in J. N. Mattavi and C. A. Amann (eds), *Combustion Modeling in Reciprocating Engines*, Plenum, New York, 1980, pp. 69–129.
28. R. Diwakar and S. H. El Tahry, 'Comparison of computed flow-fields and wall heat fluxes with measurements from motored reciprocating engine-like geometries', *Comput. Eng.*, **1**, 175–188 (1983).
29. S. H. El Tahry, 'Application of a Reynolds stress model to engine flow calculations', *Trans. ASME, J. Fluids Eng.*, **107**, 444–450 (1985).
30. D. C. Haworth and S. H. El Tahry, 'A pdf approach for multidimensional turbulent flow calculations with application to in-cylinder flows in reciprocating engines', *AIAA J.*, **29**, 208–218 (1991).
31. P. M. Najt, Personal communication, 1991.